Proceedings Paper:

Roberto P. G. E., Eduardo, Nejus, Sarunas, Yan, XiaoYan et al. (3 more authors) (2018) Axially and Radially Expandable Pneumatic Helical Soft Actuator for Robotic Implantables. In: ICRA 2018.

Axially and Radially Expandable Modular Helical Soft Actuator for Robotic Implantables

Eduardo R. Perez-Guagnelli[1*], Sarunas Nejus[1*], Jian Yu[2]
Shuhei Miyashita[3], YanQiang Liu[1,2], and Dana D. Damian[1,4]

***Abstract*— Soft robotics has advanced the field of biomedical engineering by creating safer technologies for interfacing with the human body. One of the challenges in this field is the realization of modular soft basic constituents and accessible assembly methods to increase the versatility of soft robots. We present a soft pneumatic actuator composed of two elastomeric strands that provide interdependent axial and radial expansion due to the modularity of the components and their helical arrangement. The actuator reaches 35% of elongation with respect to its initial height and both chambers achieve forces of 1N at about 19kPa. We describe the design, fabrication, modeling and benchtop testing of the soft actuator towards realizing 3D functional structures with potential medical applications. An example of application for soft medical robots is tissue regenerative for the long-gap esophageal atresia condition.**

I. INTRODUCTION

The impact of soft robotics has become visible throughout the medical field, e.g., in assistive technologies and rehabilitation [1] [2], minimally invasive surgery [3] [4] [5], implants [6], [7], and wearables [8], [9]. One of the main advantages of soft robots resides in their compliant mechanisms, which allow safe interaction with the human body, and thus, increase the wearability of technology for the treatment of various clinical conditions.

Tissue repair is one of the medical procedures that can benefit from the characteristics of soft robotics, such as dexterous yet gentle handling, palpation, and stretching. Advanced surgical tools, e.g., da Vinci robots, have been demonstrated to safely interact with organs and tissues. However, they are bulky and expensive and require the constant presence of surgeons; further, the success of interventions is highly dependent on extensive training of the surgeon to operate the complex machines. Alternatively, tissue engineering (TE) aims to restore the structure and function of a tissue using tissue regeneration methods. Typically these methods involve the stimulation of cell proliferation using chemical factors on biocompatible material substrates[10]. However, TE faces numerous challenges such as lack of vascularity in new tissue and poor mechanical compatibility [11] [12].

Mechanical stimulation of tissue has been found to have therapeutic effects in a variety of medical conditions [13], including haptics [14] and wound healing [15] in addition to tissue regeneration [16].

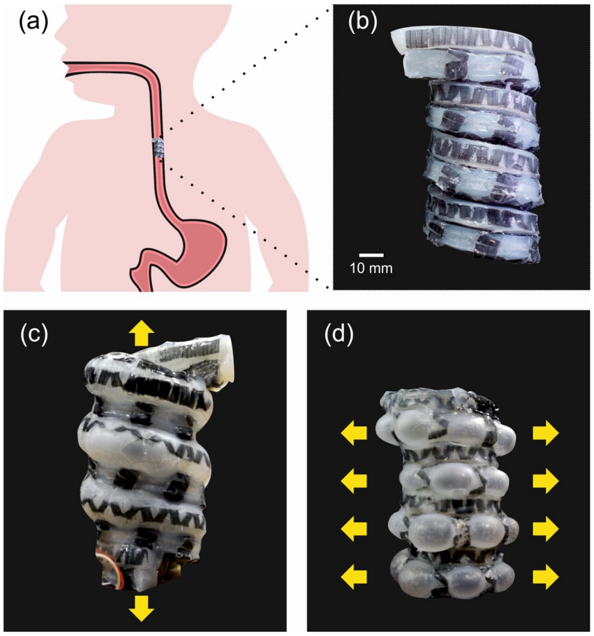

Fig. 1. The developed soft actuator for mechanostimulation-based tissue regeneration. (a) Its possible use inside the esophagus to treat the long-gap condition, (b) a view of the actuator in the relaxed state, (c) axially expanded, and (d) radially expanded.

Soft robotic implants have the potential to combine the advantages of these fields: inducement of cell proliferation to grow tissue from TE, controllability of surgical robotics, and mechanical compliance of soft robotics for safety. Such implants can be used as alternatives or as complementary technology in these fields. Such implants may be deployed inside the body, mounted on the target tissue, where the implants will use their degree of freedom to exert controlled forces and displacements on the tissue to induce regeneration and healing.

An example of potential therapies in which robotic implants may be of use is tissue regeneration of tubular organs such as the stomach, intestine, or esophagus. Such regeneration is required for conditions such as long gap esophageal atresia (LGEA) or short bowel syndrom (SBS). LGEA is a congenital defect in which there is a gap of 3cm or more in the esophagus, preventing the food from reaching the stomach. In the current corrective approach, surgeons make an incision on the back, place sutures in the lower and upper

---

[1] Automatic Control and System Engineering Department, University of Sheffield, UK. [2] School of Mechanical Engineering and Automation, Beihang University, China. [3] Department of Electronic Engineering, University of York, UK. [4] Centre of Assistive Technology and Connected Healthcare, University of Sheffield, UK. `d.damian@sheffield.ac.uk`

[*] Eduardo Roberto Perez Guagnelli and Sarunas Nejus contributed equally.

Support for this work has been provided by the University of Sheffield and The National Council of Science and Technology of Mexico.

ends of the esophagus, connect them to the outside of the body, and apply tension daily to elongate the tissue stubs, thus increasing the length incrementally. The patient, a baby, is sedated, remaining motionless in intensive care, and X-ray imaging is performed periodically to verify progress [17]. LGOA remains a challenging condition in paediatrics [18]. Our group recently introduced robotic implants that were shown to be able to reside in the body and induce growth of esophageal tissue using mechanostimulation [16].

Challenges to increasing the versatility and producibility of robotic implantable technology include (1) material selection: increasing the mechanical compliance of the implants to the surrounding tissue to reduce inflammation [19]; (2) manufacturing and assembling processes: ease of fabrication and assembly of an implant by medical engineers and surgeons for a specific therapy; and (3) implant function: physiology-compliant robotic implants that can support multiple functions in a given tissue. Technologically, these challenges can be addressed by developing elastic and modular robotic constituents that can be easily assembled into more complex medical machines. Whereas traditional robotic systems are inflexible and difficult to adapt to different medical applications, modular robots can address these limitations in the medical field by offering clinical advantages such as reconfigurability and simple manufacturing processes [20]. Still, there have been limited advancements in this direction [21].

In this paper we present a modular and multi-modal soft actuator composed of two pneumatic strands coiling together as the basic soft constituents. Due to their arrangement and their reinforced walls, the soft actuator is capable of both axial and radial expansion. Additionally, because of their simple morphology, the soft actuator's strands are easy to scale, assemble, and customize into 3D functional structures for robotic implantables.

Our paper makes the following contributions to this area of research: (1) Introduction of the concept of coiling assembly for realizing deployable complex, compact, and modular soft robotic implantables to achieve interdependent axial and radial expansion of tissue; (2) Modeling of the pneumatic actuation strand to determine the most efficient configuration of constrained segments in terms of expansion, pressure, and uniformity; (3) A demonstration of a potential application of such a soft helical actuator, with two degrees of freedom (2DOF) for tissue regeneration based on mechanostimulation; and (4) Experiments in which we demonstrate the performance of the 2DOF helical actuator.

II. HELICAL SOFT ACTUATOR DESIGN

A. *Design requirements*

Multifunctionality: The physiological functions of tubular organs, such as morphological changes due to peristalsis, their physical characteristics, such as elasticity [22], and their anatomy, such as the arrangement of muscle fibers, make multifunctionality critical in the design criteria for robotic implant platforms. The esophagus presents two types of muscles, arranged in layers, an inner circular layer and an outer longitudinal layer [23]. Therefore, a soft actuator for use with the esophagus should be able to apply traction forces and displacements to the tissue in order to stimulate both muscle layers.

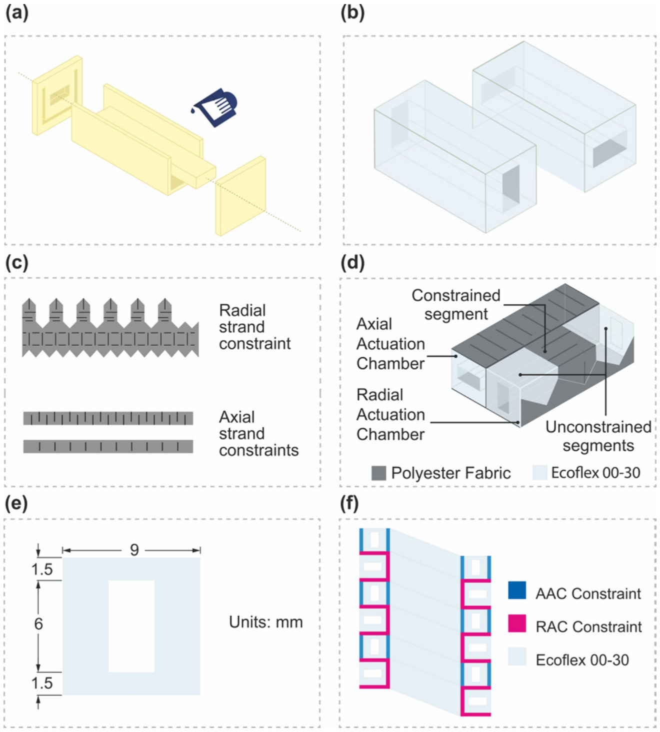

Fig. 2. Fabrication steps. (a) Design of the mold, which is made up of four parts that connect mechanically to create a hollow rectangular prism that shapes the basic structure of the pneumatic chambers; (b) the pneumatic chambers resulting from molding; (c) 2D representation of the polyester constraints for both chambers; and (d) configuration in which the polyester constraints are placed and embedded in the pneumatic chambers. The top view represents the outer surface view when these chambers are placed in helical configuration; (e) cross-sectional dimensions of the chambers; and (f) cross-sectional view of the entire helical structure. AAC and RAC are interlayered after being helically coiled in a supportive tube.

Modularity: Usually, specialized medical robotic components are non-cost effective and have limited versatility in their applications. To address these shortcomings, robotic implants should maintain functional performance across different clinical needs via morphological strategies, such as modularity. Additionally, modularity may potentially result in more complex systems due to re-configurability, scalability and ease of assembly of basic components.

B. *Conceptual Design of the Helical Actuator*

The basic modular component of the soft actuator is an elastomeric pneumatic chamber, conceptually referred to as a strand (Fig. 2 (b)). The design of the proposed actuator consists of two identical strands bonded together along their longest side. The orientation of the internal channel profile of the strand differs between adjacent strands (Fig. 2 (b)). Each strand is wrapped in polyester fabric, which constrains expansion after pressurization [24] (Fig. 2 (d)). The fabric is precut individually for each chamber to obtain specific constrained and unconstrained sections (Fig. 2 (c)). Therefore, although they have identical elastomeric morphology, they

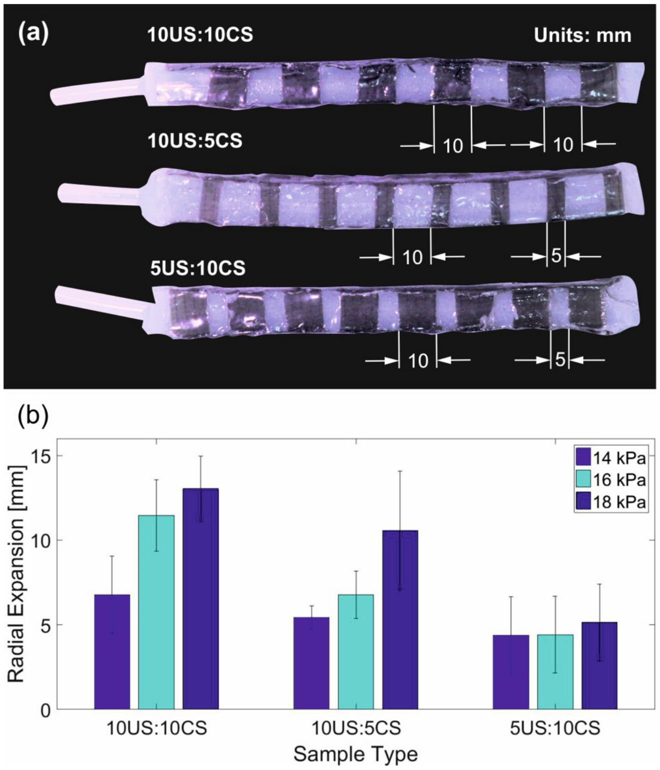

Fig. 3. Design of RAC constraints. (a) Experimental samples to determine the best configuration to maximize expansion. (b) Statistical analysis of the performance of the three samples. The sample 10US:10CS shows the most efficient configuration, as it achieves the most uniform emerging bubbles and the higher expansion across the three types of samples.

expand differently. The chambers function as elastomeric strands that are coiled together into a helical structure with interlayered actuation (Fig. 2 (f)).

The axial actuation chamber (AAC) expands to displace adjacent chambers, increasing the axial size of the actuator. The radial actuation chamber (RAC) exhibits laterally emerging bubbles from the unconstrained sections, yielding radial expansion of the actuator.

The fabric embedded in the AAC is intended to restrict radial expansion. In the RAC, it restricts axial expansion. The cuts in both cases aim to reduce shear stress during coiling of the chambers. This prevents the fabric from collapsing, increasing the compliance of the polyester. In the AAC, the sides facing both outwards and inwards are covered, while the elastomer is exposed on the upper and lower sides (Fig. 2(c)(d)). Each strand has a length of 12 cm. This conceptual design is further illustrated in the accompanying video.

C. *Design of RAC constraints*

An experiment was conducted to determine the most efficient constraint configuration. Efficiency was measured in terms of uniformity and the relation between pressure and expansion in the unconstrained sections. Three different samples were fabricated 3(a). They were each 120 mm long and the cross-section dimensions are given in Fig. 2 (e). Each configuration had a different size correlation between the fabric-constrained (CS) and fabric-unconstrained sections (US). The size ratio of each configuration in the samples was as follows: (1) 10 mm of US and 10 mm of CS; (2) 10 mm of US and 5 mm of CS; (3) 5 mm of US and 10 mm of CS.

A DC pneumatic pump was used to inflate the samples while a pressure sensor (Honeywell ASDXAVX005PGAA5) measured the changes of pressure inside the samples. Data was acquired via a NI-DAQ and processed using LabVIEW. This system is presented in more detail in Section V. Three pressure values, 14 kPa, 16 kPa, and 18 kPa, were input to each of the samples and the experiment was repeated three times per sample. Pictures were taken of the samples during the tests and while deflated. The size of the inflatable sections was measured using ImageJ software. Finally, the average size and standard deviation of the US sections were obtained from each sample at every pressure, and a plot was generated using MATLAB. Sample number one, which had equally sized US and CS, was selected as the most efficient configuration as it yielded the greatest and most uniform expansion in relation to the pressure (Fig. 3(b)).

D. *Finite Element Modeling of RAC*

In order to validate our physical experiments we modeled the mechanical behaviour of the three samples, using the ABAQUS software. The samples were made of silicone rubber, which exhibits elasticity and high non-linearity, i.e. super-elasticity. Thus, when simulating a super-elastic material in ABAQUS, the following assumptions were made: (1) the material was isotropic; (2) the material was incompressible by default; (3) the simulation included geometric non-linear effects. In this modeling, the hybrid form of the 8-node solid element C3D8RH was used. Mechanical properties of the materials were obtained by uniaxial tensile test. Using the material evaluation function of ABAQUS, the best stable Neo Hookean model was finally selected by comparing various strain energy models. The mechanical behavior of the constraint outside the actuator was simplified by modeling it as a linear elastic material. The parameters were: Young's modulus E: 2000 MPa; Poisson's ratio: 0.35. Following the parameters used in the physical experiments, FEM was conducted on three different models: (1) 10 mm of US and 10 mm of CS; (2) 10 mm of US and 5 mm of CS; (3) 5 mm of US and 10 mm of CS. The air pressure of each model was 14 kPa, 16 kPa, 18 kPa.

This modeling was intended to analyze the hydro-static deformation of the samples, so that the dynamics of the airflow into the actuator were not taken into account during the modeling process. In order to improve the convergence, the minimum analysis step was set as 0.001, and the quasi-static solution was used. The outer elastomeric surface of the chamber and the inner surface of the constraint were characterized by surface-to-surface sliding interaction and the friction coefficient was 0.5. The results of the analysis of the modeling are shown in Fig. 4. It can be seen that the sample 10US:10CS (Fig. 4 (a3)) shows to be the most efficient configuration by yielding the greatest and more uniform expansion in co-relation with pressure. This verification

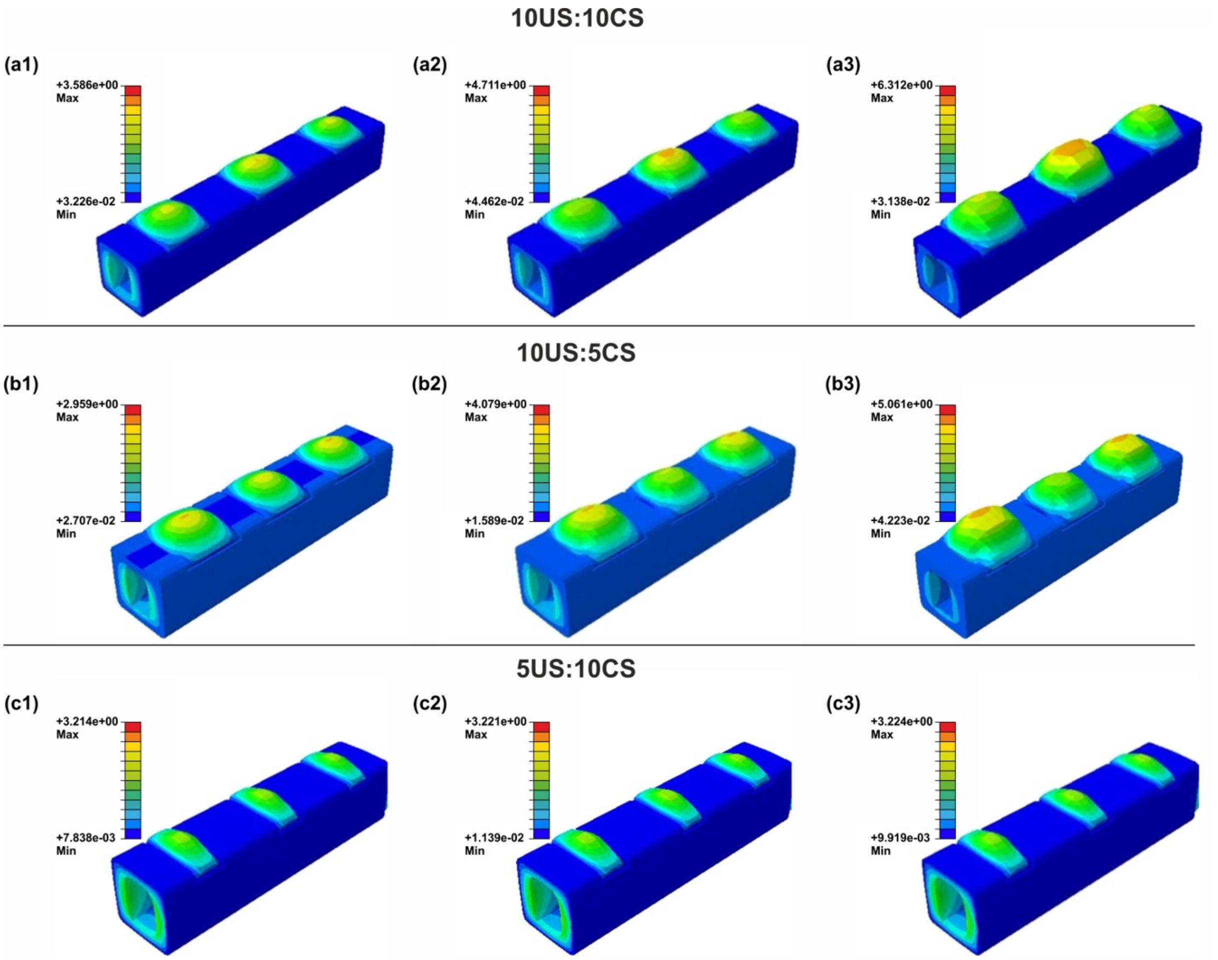

Fig. 4. Finite Element Analysis of the three elastomeric samples under 14kPa, 16kPa and 18kPa of pressure. (a1), (a2) and (a3) show the pressure response of the sample with ratio of 10US:10CS. The maximum displacement (inflation) of the bubble was 39.8%, 52.3% and 70.1% respectively; (b1), (b2) and (b3) show the pressure response of the sample with ratio of 10US:5CS. The maximum displacement of the bubble was 32.9%, 45.3%, 56.2% respectively; (c1), (c2) and (c3) show the pressure response of the sample with ratio of 5US:10CS. The maximum displacement of the bubble was 35.7%, 35.8%, 35.8% respectively.

validates our design for the RAC constraints.

III. FABRICATION OF THE ACTUATION CHAMBERS

3D printed molds (Fig. 2 (a)), fabricated in a Stratasys Mojo 3D Printing Machine out of ABS material, were used to cast the AAC and RAC. Ecoflex 00-30 (Smooth On Inc.) was mixed and defoamed using ARE-250 Mixer (Thinky), which was poured in the molds and thermally cured in the oven at 75°C for 15 minutes. Finally, the cured elastomer was disengaged from the molds (Fig. 2 (b)). Five modules were assembled together using uncured Ecoflex 00-30 to achieve a final length of each chamber of 60 cm.

The constraints were designed (Fig. 2 (c)) using AutoCAD software. Sheets of polyester were cut accordingly using a Silhouette Cameo 3 cutting machine. To embed the constraints in the AAC, we painted the thickest walls of the elastomeric structure with uncured Ecoflex 00-10, then placed one polyester sheets on each of them, and painted them again. To embed constraints in the RAC, the thicker layers of the elastomeric structure were painted manually with uncured Ecoflex 00-10 and the section of polyester with triangular cuts was aligned and embedded. The intermittent constraints aligned themselves on the top of the chamber to create the US and CS (Fig. 2 (d)). Then, all the polyester was painted in the same manner and thermally cured in the oven. The overlapping joins between constraints were secured using Ecoflex 00-30 to prevent breakage from pressurization (Fig. 2 (d)).

The two chambers were then bonded together as in (Fig. 2 (d)) using uncured Ecoflex 00-10. The helical structure was created by rolling the two chambers around a cardboard cylinder. This cylinder was covered with spray release agent, allowing it to be withdrawn and discarded without damaging the actuator after shaping the helix.

IV. INTEGRATED ANALYTICAL MODEL OF THE HELICAL ACTUATOR

In this section, we introduce a simple analytical model of the entire actuator to understand the relation between the physical components and their mechanical response to pressurization. For this actuator, the main performance metrics are the drive force and the displacement. In terms of radial

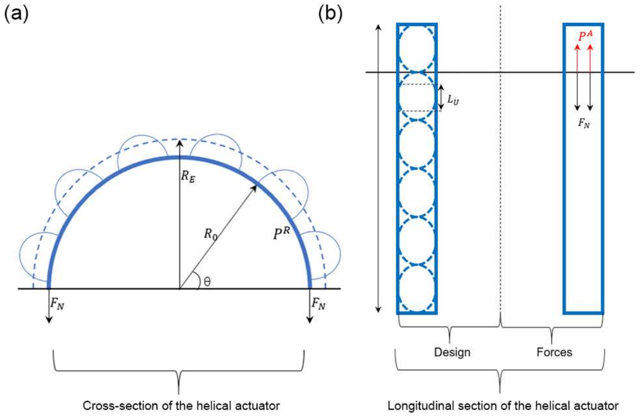

Fig. 5. Simplified (a) radial and (b) axial expansion models.

expansion, we simplified the helix as a circle. We cut the circle in half and mark all the forces, as shown in Fig. 5 (a). Then, we obtained the force balance equation, as shown in Eq. 1.

$$\frac{ES^R(R_E - R_0)}{R_0} = \int_0^{\pi} (P^R - P^S)L_u R_0 \sin\theta d\theta \qquad (1)$$

where E is the Young's modulus of the material, S^R is the cross-sectional area of the rectangular unit, R_0 is the initial radius, R_E is the equivalent radius after radial expansion, P^R is the radial pressure, P^S is the standard atmospheric pressure and L_u is the side length of the rectangular unit Fig. 5 (b). Eq. 1 can be simplified as Eq. 2.

$$R_E - R_0 = \frac{2(P^R - P^S)R_0^2 L_u}{ES^R} \qquad (2)$$

In terms of axial expansion, we can simplify the actuator as a cylinder. The displacement is achieved by the length-wise extension of the cylinder. An assumption is made that the circumference wall does not deform in the radial direction. We cut the longitudinal section as in Fig. 5 (b). Because the elongation of the actuator is achieved by deformation of the top and bottom walls of the rectangular unit, the side wall is assumed to be rigid, and therefore the effective extended height is less than the actual length. Then we cut the top section to analyze the force; the force balance equation is shown in Eq. 3:

$$F + ES^A \frac{\delta L}{NL_{uE}} = (P^A - P^S)S^T \qquad (3)$$

where P^A is the axial pressure, P^S is the standard atmospheric pressure S^T is the drive area of the cross section, E is the Young's modulus of the material, S^A is the cross-sectional area of the cylinder, L_{uE} is the equivalent length of L_u for the elongation, N is the coil count, and δL is the height elongation. From Eq. 3, we find that both the axial force and the displacement have linear relationships with the input pressure. Similar curves are shown in the experimental section.

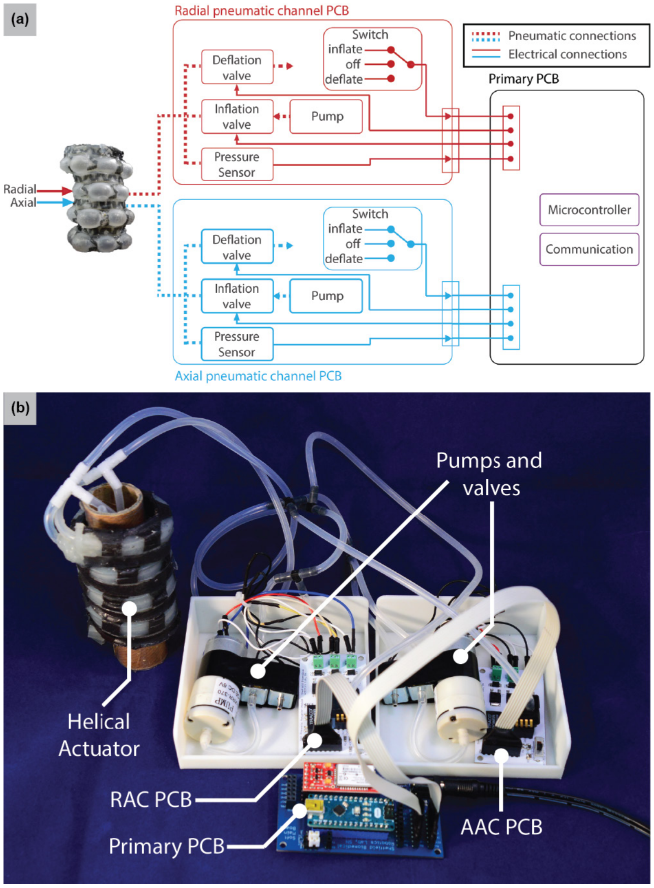

Fig. 6. Electrical design. (a) Electrical design topology, (b) electrical setup with the helical actuator connected.

V. CONTROL SETUP

The system is comprised of two pneumatically actuated chambers: axial and radial. Modular circuit boards were designed for ease of use and reliability. The primary printed circuit boards (PCB) houses the microcontroller, power input, and communication, while dedicated auxiliary boards include the pneumatic components, one for each of the chambers. The primary board provides connections for three separately actuated pneumatic channels, taking into account a possible extension of the design in the future. Figure 6(a) illustrates the general electrical topology, including our electrical control and feedback as well as pneumatic connections. Figure 7 provides an overview of the designed PCBs.

Each of RAC and AAC have a dedicated DC pump (XRR-370) and two normally closed solenoid valves (FA0520D) for inflation and deflation. Inflation is achieved by the pumps and deflation is achieved by opening the corresponding valve and exhausting the air from the actuator. The valves are controlled by independent digital signals from the microcontroller (Arduino Nano). Because the valves and pumps require currents as high as 300mA, they are interfaced with the microcontroller through MJD112G NPN transistors. The inflation or deflation of each chamber is triggered manually by two SP3T slide switches (C&K Components

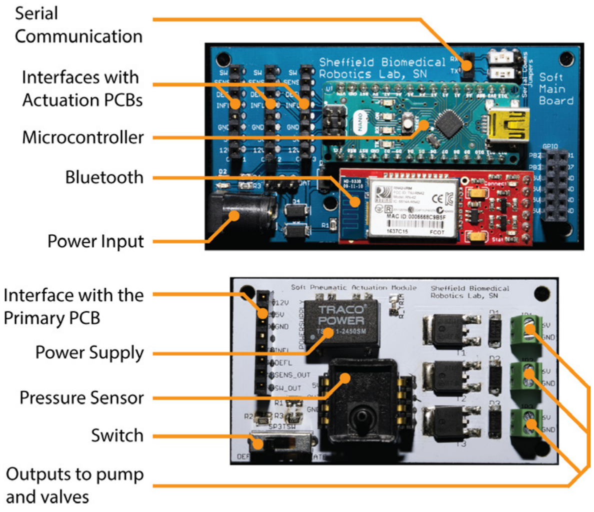

Fig. 7. Overview of the main and auxiliary control PCBs.

OS103011MS8QP1).

The circuit can be powered by either a 12V/3A power supply (XP POWER VEP36US12) or a rechargeable battery pack (for example 8 x eneloop AAA batteries, providing 9.6V to the system). The design was based on the low-cost electro-pneumatic circuit developed by the Soft Robotics Toolkit. Figure 6(b) shows the entire setup, where the helical actuator is interfaced through two of the three available pneumatic channels. Using this circuit, the two actuator chambers could be inflated independently or jointly.

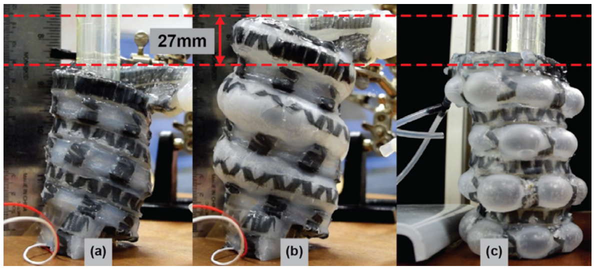

Fig. 8. Actuator state: (a) relaxed, (b) axial chamber inflated, (c) radial chamber inflated.

VI. EXPERIMENTS

In order to evaluate the independent and interdependent characteristics of the helical soft pneumatic actuator, three sets of experiments were conducted. First, RAC performance was evaluated by measuring the force exhibited against an external spatial constraint. Second, AAC performance was assessed in two separate experiments by measuring the force exhibited against an external constraint as well as the maximum freeload AAC expansion achieved. Finally, the interdependence between AAC and RAC was appraised by maintaining one of the chambers at constant pressure while pressurizing the other and vice versa. Associated changes in the pressures and forces of the chambers were evaluated. An exemplification of the independent inflation performance of the two chambers is illustrated in Fig. 8.

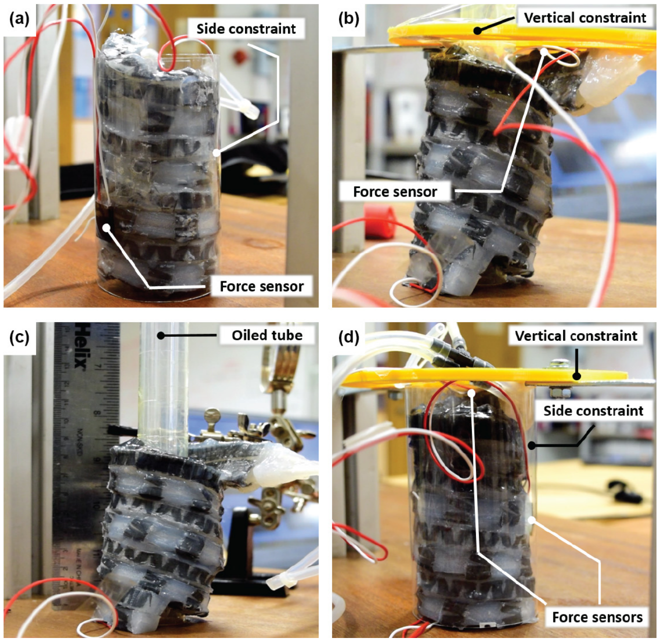

Fig. 9. Experimental setups: (a) radial force measurement, (b) axial force measurement, (c) axial displacement, and (d) radial and axial force; interaction of both chambers.

The air pressure within the chambers was tracked by Honeywell ASDXAVX005PGAA5 sensors, which were connected to a data acquisition system (cDAQ-9178 DAQ platform with NI9201 module, National Instruments). Data was acquired through LabView and later processed and visualized in MATLAB.

A. Performance of the RAC

The first experiment aimed to measure the radial force exhibited by RAC inflation. The implant was covered with a rigid polyethylene terephthalate (PET) cylinder holding a force sensor that was adhered to its inner surface and in direct contact with the bubbles emerging from the RAC, to measure the applied forces, as shown in Fig. 9(a). The force sensor was previously calibrated and data was acquired at a frequency of 3Hz. The force sensor measured the amount of force with which one of the emerging balloons pressed against the rigid case, caused by increasing pressure within the RAC. AAC was kept in a relaxed state. Figure 10 shows the experimental results. The force sensor's initial contact with the actuator has a force of 0.25N. With increasing pressure in the chamber, the measured force increased in an approximately linear fashion, eventually reaching 1N at 20kPa pressure within the chamber.

B. Actuation of the axial chamber

The second set of experiments evaluated force and freeload elongation achieved by AAC pressurization. First, the axial force was recorded by by placing a force sensor on the top of the actuator and restricting the actuator's axial movement via a flat horizontal plate fixed above it (Fig. 9(b)). Second, elongation was determined by placing the actuator around

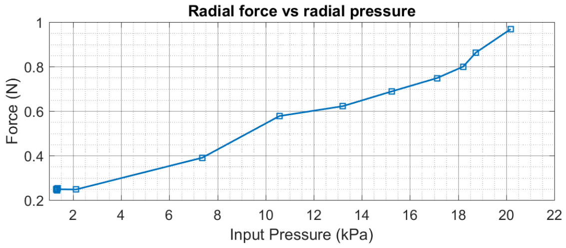

Fig. 10. Force exhibited against the external spatial constraint during RAC pressurization

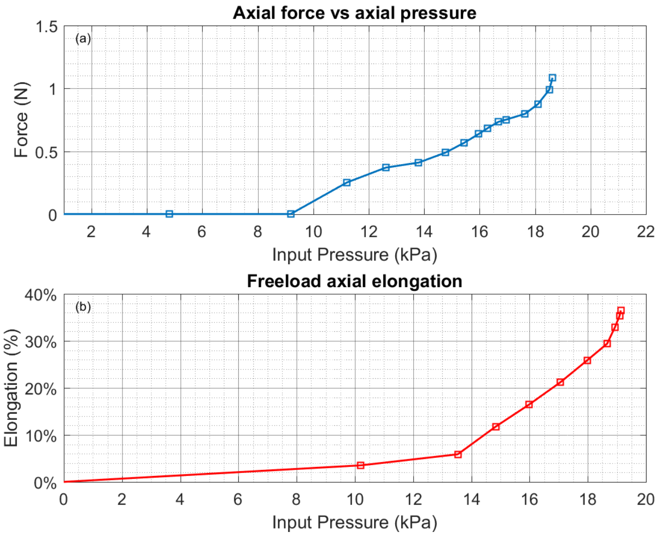

Fig. 11. Axial performance of the actuator (a) AAC force; (b) freeload axial elongation.

an oiled (Cole Parmer Vacuum Pump Oil CP 500) plastic tube (Fig. 9(c)) that supported the actuator vertically without restricting its movement. A ruler was placed alongside the actuator, and a Nikon D5300 camera was used to track and record the displacement. The readings were recorded manually from the video in 1s steps and synchronized with the digital pressure readings. The RAC was not actuated during this experiment.

The graph in Fig. 11(a) shows that the force did not start rising until the AAC pressure reached 9kPa. This is because the initial placement of the sensor allowed a small gap between the actuator and the yellow restriction plate. After reaching the aforementioned pressure, the actuator expanded sufficiently to touch the plate where the sensor was mounted. Subsequently, further increase in AAC pressure up to 19kPa resulted in the actuator exerting 1N force against the plate.

The elongation measurement showed a 35% increase in the height of the actuator (with respect to its initial height of 85mm), as reflected in Fig. 11(b).

C. Interdependence of RAC and AAC

Because the actuator's radial and axial chambers are interdependent, the final experiment aimed to exemplify and quantify the changes in *RAC force and pressure* due to *AAC actuation* and vice versa. In Fig. 12(a), the period from 0s to 20s shows the initial AAC pressure of 14kPa, which gave rise to 0.8N of axial force and 0.4N of radial force. Subsequently, the RAC was pressurized in two steps (at 21s and 30s), eventually reaching 18kPa. This gave rise to not only to radial force (0.8 N final value, +0.4N change) but also to axial force (1.2N final value, +0.4N change). Moreover, a slight increase in the axial pressure (+2kPa) was identified. This proves that the AAC is dependent on the pressurization of the RAC.

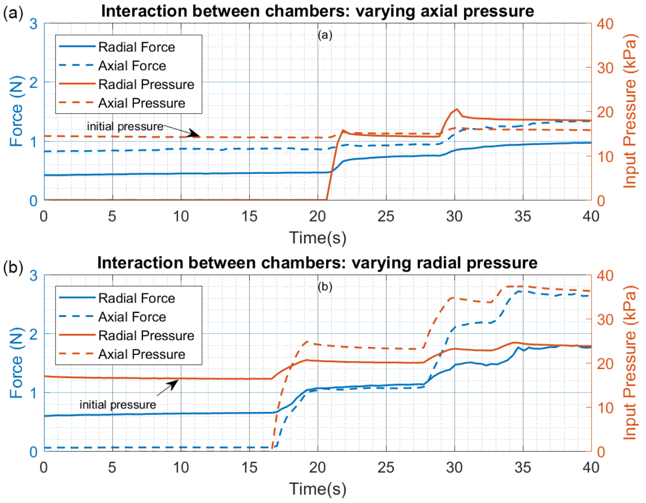

Fig. 12. Interaction between both chambers. (a) AAC was initially held constant at 14kPa while pressure in the AAC was increased, (b) RAC held constant at 16kPa while pressure in the RAC increased. Both experiments showed changes in radial and axial forces.

Results from a corresponding experiment in which the RAC pressure was held constant at 16kPa are given in Fig. 12(b). Initial pressurization of the RAC resulted in an initial radial force of 0.6N. The axial force was unaffected until the axial chamber's input pressure began rising at t = 17s, finally reaching 37 kPa. A similar effect as in the previous experiment can be observed here: AAC pressurization results in an increase in both the axial (+2.6N) and radial (+0.8N) forces, as well as an increase in radial pressure (+8kPa).

VII. DISCUSSION & CONCLUSION

This work shows a novel modular method for assembling coiled elastomeric chambers that act as strands of a complex soft machine. Its capabilities as an axially and radially expandable pneumatic helical soft actuator were demonstrated here, showing its potential usefulness in biomedical applications, such as implants for tissue growth. The basic modules that shape the soft platform and their 3-step fabrication represent an opportunity for development of reconfigurable soft structures that are operable across multiple clinical applications, exploiting the therapeutical effect of mechanostimulation.

Based on the experimental results, both the RAC and the AAC can achieve significant forces, ranging up to 3N against spatial constraints when pressurized. The independent maximum extension of the AAC was evaluated as 35% of its initial length. The actuator can thus be applied to treat LGEA by utilizing the AAC for regeneration of muscle fibers that are longitudinally oriented, whereas the RAC can support the regeneration of muscle fibers that are radially oriented. Additionally, the RAC can help to maintain the natural ratio of the lumen in tubular organs, such as the esophagus.

The two actuator chambers are interdependent. While this might initially be considered a negative, deploying both chambers together achieved higher forces against the external spatial constraints than those achieved in the first two experiments, in which the AAC and RAC were pressurized independently. Whether this side effect is more of a benefit or a disadvantage, however, depends largely on the application, and therefore further refinements must take this characteristic into account. Therefore, further research will explore control of the interdependence of the chambers to achieve two different target stimulation forces and how to maximize these forces. Likewise, developing standardized methods for fabrication and miniaturization and extending the modularity of the platform for other organ sizes and shapes represent significant opportunities for future development.

ACKNOWLEDGMENT

We thank Flavien Lefevre and Ghibson Hudson for their help with the manuscript; XianYou Yan for his help with modeling and Manuela Garcia Hoyos for helping with the experiments for the design of RAC constraints.

REFERENCES

[1] L. N. Awad, J. Bae, K. Odonnell, S. M. De Rossi, K. Hendron, L. H. Sloot, P. Kudzia, S. Allen, K. G. Holt, T. D. Ellis *et al.*, "A soft robotic exosuit improves walking in patients after stroke," *Science translational medicine*, vol. 9, no. 400, p. eaai9084, 2017.

[2] P. Polygerinos, K. C. Galloway, E. Savage, M. Herman, K. O'Donnell, and C. J. Walsh, "Soft robotic glove for hand rehabilitation and task specific training," in *Robotics and Automation (ICRA), 2015 IEEE International Conference on*. IEEE, 2015, pp. 2913–2919.

[3] K. P. Sajadi and H. B. Goldman, "Robotic pelvic organ prolapse surgery," *Nat. Rev. Urol.*, vol. 12, no. 4, pp. 216–24, 2015.

[4] S. Miyashita, S. Guitron, K. Yoshida, S. Li, D. D. Damian, and D. Rus, "Ingestible, controllable, and degradable origami robot for patching stomach wounds," in *Robotics and Automation (ICRA), 2016 IEEE International Conference on*. IEEE, 2016, pp. 909–916.

[5] H. M. Le, T. N. Do, and S. J. Phee, "A survey on actuators-driven surgical robots," *Sensors and Actuators A: Physical*, vol. 247, pp. 323–354, 2016.

[6] E. T. Roche, M. A. Horvath, I. Wamala, A. Alazmani, S.-E. Song, W. Whyte, Z. Machaidze, C. J. Payne, J. C. Weaver, G. Fishbein, J. Kuebler, N. V. Vasilyev, D. J. Mooney, F. A. Pigula, and C. J. Walsh, "Soft robotic sleeve supports heart function." *Sci. Transl. Med.*, vol. 9, no. 373, pp. 1–12, 2017.

[7] D. D. Damian, S. Arabagi, A. Fabozzo, P. Ngo, R. Jennings, M. Manfredi, and P. E. Dupont, "Robotic implant to apply tissue traction forces in the treatment of esophageal atresia," *Robotics and Automation (ICRA), 2014 IEEE International Conference on. IEEE, 2014.*, no. 1, pp. 786–792, 2014.

[8] P. Bonato, "Advances in wearable technology and applications in physical medicine and rehabilitation." *J. Neuroeng. Rehabil.*, vol. 2, no. 1, p. 2, 2005.

[9] Y.-L. Park, B.-r. Chen, N. O. Pérez-Arancibia, D. Young, L. Stirling, R. J. Wood, E. C. Goldfield, and R. Nagpal, "Design and control of a bio-inspired soft wearable robotic device for ankle–foot rehabilitation," *Bioinspiration & biomimetics*, vol. 9, no. 1, p. 016007, 2014.

[10] A. Atala, F. K. Kasper, and A. G. Mikos, "Engineering complex tissues." *Sci. Transl. Med.*, vol. 4, no. 160, p. 160rv12, 2012.

[11] F. J. O'brien, "Biomaterials & scaffolds for tissue engineering," *Materials today*, vol. 14, no. 3, pp. 88–95, 2011.

[12] R. Nigam and B. Mahanta, "An overview of various biomimetic scaffolds: Challenges and applications in tissue engineering," *Journal of Tissue Science & Engineering*, vol. 5, no. 2, p. 1, 2014.

[13] C. Huang, J. Holfeld, W. Schaden, D. Orgill, and R. Ogawa, "Mechanotherapy: Revisiting physical therapy and recruiting mechanobiology for a new era in medicine," *Trends Mol. Med.*, vol. 19, no. 9, pp. 555–564, 2013.

[14] D. D. Damian, M. Ludersdorfer, Y. Kim, A. H. Arieta, R. Pfeifer, and A. M. Okamura, "Wearable haptic device for cutaneous force and slip speed display," in *Robotics and Automation (ICRA), 2012 IEEE International Conference on*. IEEE, 2012, pp. 1038–1043.

[15] L. Lancerotto and D. P. Orgill, "Mechanoregulation of angiogenesis in wound healing," *Advances in wound care*, vol. 3, no. 10, pp. 626–634, 2014.

[16] D. D. Damian, K. Price, S. Arabagi, I. Berra, Z. Machaidze, S. Manjila, S. Shimada, A. Fabozzo, G. Arnal, D. Van Story *et al.*, "In vivo tissue regeneration with robotic implants," *Science Robotics*, vol. 3, no. 14, p. eaaq0018, 2018.

[17] D. D. Damian, S. Arabagi, A. Fabozzo, P. Ngo, R. Jennings, M. Manfredi, and P. E. Dupont, "Robotic implant to apply tissue traction forces in the treatment of esophageal atresia," *in Robotics and Automation (ICRA), 2014 IEEE International Conference on. IEEE, 2014.*, no. 1, pp. 786–792, 2014.

[18] D. Wanaguru, C. Langusch, U. Krishnan, V. Varjavandi, A. Jiwane, S. Adams, and G. Henry, "Is fundoplication required after the foker procedure for long gap esophageal atresia?" *Journal of pediatric surgery*, vol. 52, no. 7, pp. 1117–1120, 2017.

[19] P. Moshayedi, G. Ng, J. C. F. Kwok, G. S. H. Yeo, C. E. Bryant, J. W. Fawcett, K. Franze, and J. Guck, "The relationship between glial cell mechanosensitivity and foreign body reactions in the central nervous system," *Biomaterials*, vol. 35, no. 13, pp. 3919–3925, 2014.

[20] S. Chennareddy, A. Agrawal, and A. Karuppiah, "Modular self-reconfigurable robotic systems: A survey on hardware architectures," *Journal of Robotics*, vol. 2017, 2017.

[21] G. Agarwal, N. Besuchet, B. Audergon, and J. Paik, "Stretchable materials for robust soft actuators towards assistive wearable devices," *Scientific reports*, vol. 6, p. 34224, 2016.

[22] L. R. Versteegden, K. A. Van Kampen, H. P. Janke, D. M. Tiemessen, H. R. Hoogenkamp, T. G. Hafmans, E. A. Roozen, R. M. Lomme, H. van Goor, E. Oosterwijk *et al.*, "Tubular collagen scaffolds with radial elasticity for hollow organ regeneration," *Acta biomaterialia*, vol. 52, pp. 1–8, 2017.

[23] V. Mahadevan, "Anatomy of the oesophagus," *Surgery-Oxford International Edition*, vol. 35, no. 11, pp. 603–607, 2017.

[24] F. Ilievski, A. D. Mazzeo, R. F. Shepherd, X. Chen, and G. M. Whitesides, "Soft robotics for chemists," *Angewandte Chemie*, vol. 123, no. 8, pp. 1930–1935, 2011.